CrossMark

Numerical simulation of the seismic liquefaction mechanism in an offshore loosely deposited seabed

Jianhong Ye[1,2] · Gang Wang[2]

Abstract As a natural foundation of offshore structures, the instability of offshore seabed foundations is the dominant factor for the failure of offshore structures in strong earthquake events. It has been reported that a great number of offshore structures have failed due to soil liquefaction of Quaternary loosely deposited seabed during several recent strong seismic events. At present, countless investigations on seismic wave-induced liquefaction in on-land soil have been conducted. However, investigations on seismic wave-induced seabed soil liquefaction in an offshore environment is limited. In this study, a coupled numerical model [fluid–structure–seabed interaction (FSSI)-CAS 2D] was utilized to investigate the seismic wave-induced liquefaction mechanism in newly deposited seabed soil. The advanced soil constitutive model PZIII was adopted to describe the nonlinear dynamic behavior of loose soil. In computation, the variation of void ratio e, and related variation of soil permeability is taken into consideration; and the hydrostatic pressure acting on the seabed surface, as a boundary condition value, is automatically updated based on seabed deformation. The numerical results indicate that a loose seabed could liquefy completely, and that seabed soil liquefaction initiates at the surface of the seabed, then progresses downward. It is also indicated that the advanced soil constitutive model, Pastor–Zienkiewicz Mark III (PZIII), is capable of describing the post-liquefaction behavior of loose seabed soil to some extent.

Keywords Offshore loose sediments · Quaternary seabed soil · Seismic dynamics · Progressive liquefaction · Pore pressure build up · Japanese 311 off-Pacific coast earthquake

Introduction

During the last two decades, more and more marine structures, such as breakwaters, oil platforms and turbines have been constructed on seabed floors in offshore areas. The stability of these constructed marine structures under environmental loading is the main concern for ocean engineers. Generally, there are two types of environmental loading in an offshore area: endless ocean waves, and possible earthquakes. Ocean waves are a conventional form of loading for all marine structures. Their effect on the stability of marine structures has been widely investigated (Ye 2012a). However, little attention has been paid to the earthquake-induced liquefaction of seabed, as well as the seismic stability of offshore structures. In fact, it was reported (Sumer et al. 2007; Groot et al. 2006) that a great number of offshore structures have failed due to seabed liquefaction during several recent strong earthquake events, such as the Turkey Kocaeli Earthquake in 1999 ($M_L = 7.4$), and the Japan Tokachi-oki earthquake in 2003 ($M_L = 8.0$). To date, countless investigations on seismic soil liquefaction on land have been conducted, adopting shaking table tests (Ye et al. 2007), centrifuge modelling (Bao et al. 2014) and numerical simulation (Huang et al. 2008; Heider et al. 2014; Xia et al. 2010; Huang et al. 2012). As a result, the recognition of soil liquefaction on land has been significantly improved (Huang and Yu 2013). However, investigations on the

✉ Jianhong Ye
yejianhongcas@gmail.com

1 State Key Laboratory of Geomechanics and Geotechnical Engineering, Institute of Rock and Soil Mechanics, Chinese Academy of Sciences, Wuhan 430071, China

2 Department of Civil and Environment Engineering, The Hong Kong University of Science and Technology, Ngan Ying Rd, Clear Water Bay, Hong Kong

🌀 Springer

mechanism and characteristics of seismic wave-induced soil liquefaction of offshore seabed is limited. Among the limited literature, Ye (2012c) and Ye and Jeng (2013) investigated the nonlinear dynamics, and momentary liquefaction of a seabed foundation under an offshore breakwater in a strong earthquake event. However, the seabed foundation is limited to very dense soil (only elastic deformation exists). Some researchers, for example, Jafarian et al. (2010), investigated the seismic dynamics of a breakwater and its seabed foundation, adopting an elasto-plastic model; however, only simple constitutive soil models, for example, the Mohr–Coulomb model, were adopted to describe soil behavior under seismic loading. Obviously, it is insufficient to understand the liquefaction characteristics in loose seabed triggered by seismic waves.

In offshore environments, the newly deposited Quaternary seabed soil widely exists in the world. Actually, a great number of offshore engineered structures are built on Quaternary sediments. The particle arrangement of Quaternary seabed soil generally is relatively loose, far from being very dense. Under cyclic loading (magnitude is greater than a critical value), soil particles re-arrange their relative positions to a more dense status, accompanying a pore water drainage process. In this process, pore water pressure builds up, making soil liquefy, or soften. Therefore, it is very dangerous to build a marine structure (breakwater, turbine, pipeline, oil platform, etc.) on newly deposited Quaternary seabed floors. Here, we take the Quaternary loose seabed soil as a typical example to investigate the mechanism and characteristics of seismic wave-induced liquefaction in loose seabed sediments.

In this study, taking a coupled numerical model [fluid–structure–seabed interaction (FSSI)-CAS 2D; Ye et al. 2013] as the tool, the seismic wave-induced liquefaction of less dense seabed is investigated. The advanced soil constitutive model Pastor–Zienkiewicz Mark III (PZIII) proposed by Pastor et al. (1990) is used to discribe the complicated nonlinear dynamic behaviour of loose seabed soil, rather than the simple Mohr–Coulomb model. The variation of void ratio e, and corresponding permeability k of soil is novelly considered in this computation. Additionally, the hydrostatic pressure acting on the seabed floor as the boundary value is also updated based on seabed deformation. A real recorded seismic wave during the Japan 311 off-Pacific coast strong earthquake event is adopted as the input excitation.

Coupled numerical model: FSSI-CAS 2D

Governing equation

The dynamic Biot's equations known as "$u - p$" approximation proposed by Zienkiewicz et al. (1980) are used to govern the dynamic response of the porous seabed soil under seismic wave loading:

$$\frac{\partial \sigma_x'}{\partial x} + \frac{\partial \tau_{xz}}{\partial z} = -\frac{\partial p_s}{\partial x} + \rho \frac{\partial^2 u_s}{\partial t^2}, \tag{1}$$

$$\frac{\partial \tau_{xz}}{\partial x} + \frac{\partial \sigma_z'}{\partial z} + \rho g = -\frac{\partial p_s}{\partial z} + \rho \frac{\partial^2 w_s}{\partial t^2}, \tag{2}$$

$$k \nabla^2 p_s - \gamma_w n \beta \frac{\partial p_s}{\partial t} + k \rho_f \frac{\partial^2 \epsilon_v}{\partial t^2} = \gamma_w \frac{\partial \epsilon_v}{\partial t}, \tag{3}$$

where (u_s, w_s) = the soil displacements in the horizontal and vertical directions, respectively; n = soil porosity; σ_x' and σ_z' = effective normal stresses in the horizontal and vertical directions, respectively; τ_{xz} = shear stress; p_s = the pore water pressure; $\rho = \rho_f n + \rho_s(1 - n)$ is the average density of a porous seabed; ρ_f = the fluid density; ρ_s = solid density; k = Darcy's permeability; g = is the gravitational acceleration; γ_w is the unit weight of water; and ϵ_v is the volumetric strain. In Eq. (3), the compressibility of pore fluid (β) and the volumetric strain (ϵ_v) are defined as

$$\beta = \left(\frac{1}{K_f} + \frac{1 - S_r}{p_{w0}}\right), \quad \text{and} \quad \epsilon_v = \frac{\partial u_s}{\partial x} + \frac{\partial w_s}{\partial z}, \tag{4}$$

where S_r = the degree of seabed saturation, p_{w0} = the absolute static pressure, and K_f = the bulk modulus of pore water, generally, $K_f = 2.24 \times 10^9$ N/m^2. Here, the compressibility of pore fluid β is taken to consider the unsaturated state of seabed soil, which is only applicable for nearly saturated soil. In fact, the saturation of seabed soil in offshore areas generally is >90 %, which is in the application range of β.

The finite element (FE) method is used to solve the above governing equation (1)–(3), and the generalized Newmark pth order scheme for the jth order equation scheme (implicit scheme) is adopted to calculate time integration when solving the above governing equations (Chan 1988a). For the problem of FSSI, a coupled numerical model (FSSI-CAS 2D) was developed by Ye (2012a). In FSSI-CAS 2D, the volume average Reynolds-average Navier–Stokes (VARANS) equation (Hsu et al. 2002) governs wave motion and porous flow in porous seabeds, and the above dynamic Biot's equation governs the dynamic behaviour of an offshore structure and its seabed foundation. A coupled algorithm was developed to couple the VARANS equation and Biot's dynamics equation together. More detailed information about the coupled model can be found in Ye et al. (2013), Ye (2012a) and Zienkiewicz et al. (1999). Based on FSSI-CAS 2D, an earthquake modulus was further developed to investigate the seismic dynamics of offshore structures, recently (Ye and Wang 2015).

From the point of view of physics, void ratio e and related Darcy's permeability k of soil vary based on the

deformation characteristics of granular materials. In the most previous investigation, this variation process generally is not considered to be based on a small deformation assumption, namely, void ratio e and permeability k remain constant. In this earthquake modulus, the seismic wave-induced variation of void ratio of a seabed soil can be considered by the following formulation: $e_{n+1} = (1 + e_n) \exp\left(\frac{\Delta p}{Q} + \Delta\epsilon_{vs}\right) - 1$, which is established from the prospect of large deformation, where n stands for the nth time step, Δp is the incremental pore pressure, $\Delta\epsilon_{vs}$ is the incremental volumetric strain of soil, and $Q = 1/\beta$ is the compressibility of pore water. Correspondingly, the permeability of seabed soil k varies following $k = C_f \frac{e^3}{1+e}$, where C_f is an empirical coefficient determined by $C_f = k_0 \frac{1+e_0}{e_0^3}$ (Miyamoto et al. 2004). Additionally, the hydrostatic water pressure acting on the seabed floor, as the boundary values in the FE computation, is changeable based on the seismic wave-induced deformation of the seabed foundation. Under seismic loading, the void ratio of a loose seabed soil will decrease, leading to the subsidence of the seabed surface. As a result, the hydrostatic pressure acting on the seabed surface would change significantly, especially in the cases involving large deformation. The practice of numerical implementation in this study indicated that the change of hydrostatic pressure on the seabed surface should be considered according to subsidence; Otherwise, non-convergence may be encountered in numerical analysis.

In FSSI-CAS 2D, an excellent soil model (PZIII) proposed by Pastor et al. (1990) was adopted to describe the dynamic behavior of loose seabed soil under seismic wave loading. In PZIII, the yield surface function f and plastic potential surface function g are respectively defined as:

$$f = q' - M_f p'\left(1 + \frac{1}{\alpha_f}\right)\left[1 + \left(\frac{p'}{p'_f}\right)^{\alpha_f}\right] = 0 \tag{5}$$

$$g = q' - M_g p'\left(1 + \frac{1}{\alpha_g}\right)\left[1 + \left(\frac{p'}{p'_g}\right)^{\alpha_g}\right] = 0 \tag{6}$$

The plastic modulus at the loading and unloading stages is defined as:

$$H_L = H_0 p'\left(1 - \frac{q'/p'}{\eta_f}\right)^4$$
$$\times \left[1 - \frac{q'/p'}{M_g} + \beta_0\beta_1 exp(-\beta_0\xi)\right]\left(\frac{q/p'}{\eta_{\max}}\right)^{-\gamma_{DM}} \tag{7}$$

$$H_U = \begin{cases} H_{u0}\left(\dfrac{M_g}{\eta_u}\right)^{\gamma_U} & \text{for } \left|\dfrac{M_g}{\eta_u}\right| > 1 \\[3mm] H_{u0} & \text{for } \left|\dfrac{M_g}{\eta_u}\right| \leq 1 \end{cases} \tag{8}$$

where the p' and q' are the mean effective stress and deviatoric stress, respectively. M_f, M_g, α_f, α_g, β_0, β_1, γ and γ_{DM} are the parameters describing the properties of sandy soil. For simplicity, the definition of other parameters can be referred to Pastor et al. (1990) and Zienkiewicz et al. (1999). The reliability of PZIII has been validated by a series of laboratory tests involving monotonic and cyclic loading, especially by the centrifuge tests in the "Verification of Liquefaction Analysis by Centrifuge Studies" (VELACS) project (Zienkiewicz et al. 1999). This model was one of the heritages of Olek Zienkiewicz (Pastor et al. 2011). The coupled model FSSI-CAS 2D used in this study also has been validated by an analytical solution, and a series of laboratory wave flume tests. The earthquake modulus in FSSI-CAS 2D was developed based on a widely validated geotechnical FE code (Chan 1988b). Therefore, the reliability of the earthquake modulus in FSSI-CAS 2D can be guaranteed.

Boundary condition and input seismic wave

In this study, a flat seabed in an offshore environment was chosen as the investigation object. The thickness of the seabed was 20 m, and the length of computation domain was 200 m. In computation, the following boundary conditions were applied:

1. The bottom of the seabed foundation is impermeable:

$$\frac{\partial p_s}{\partial z} = 0 \quad \text{at} \quad z = 0 \tag{9}$$

2. A laminar boundary condition was applied on the two lateral sides of the computational domain. Under this condition, there was no reflection on the lateral sides, and the two lateral sides can freely deform. This boundary also makes the computational domain horizontally infinite.

3. Hydrostatic pressure was applied on the surface of seabed. In each time step, the hydrostatic pressure acting on seabed floor, which was the boundary value on the seabed surface, was updated as

$$p_s = p_0 + \rho g s_v = \rho g d_0 + \rho g s_v \tag{10}$$

where d_0 is the initial water depth, and s_v is the vertical subsidence of points on the seabed floor resulting from seismic loading.

4. Input horizontal and vertical seismic accelerations waves are input at the bottom of the computational domain simultaneously.

A seismic wave recorded in an offshore environment serves best as the input seismic wave. Here, the recorded underground seismic wave at the observation station MYGH03

(141.6412E, 38.9178N) in the Japan 311 off-Pacific coast of Tohoku earthquake ($M_L = 9.0$) was adopted as the input seismic wave. The distance from this chosen observation station to the epicenter (142.9E, 38N) was 154 km. MYGH03 was near to the coastal line of Pacific ocean. Therefore, the chosen input seismic wave here was similar as close as possible with a real seismic wave propagating to an offshore area. In Fig. 1, it can be seen that the displacements were zero when the acceleration wave ended; and the peak ground acceleration (PGA) was 1.33 m/s^2 in the E–W direction, and 1.21 m/s^2 in the U–D direction.

In this seismic dynamics computation, the stiffness–proportional Rayleigh damping model was applied for the purpose of stabilizing the numerical results. In the Rayleigh damping model, the viscous damping matrix [C] is related to the mass matrix [M] and initial stiffness matrix [K] as

$$[C] = \alpha[M] + \beta[K] \tag{11}$$

where α and β are two coefficients, which can be determined by the viscous damping ratio and the period of input dynamic loading. In this study, $\alpha = 0$, and $\beta = 0.0003$ were chosen as that in Wang and Sitar (2011).

Seismic dynamics of the seabed

The model parameters of loosely deposited seabed soil for the PZIII constitutive model are listed in Table 1, which were determined by Zienkiewicz et al. (1999) for Nevada sand ($D_r = 60\,\%$) when attending the VELACS project hosted by American National Science Foundation (NSF). Actually, these model parameters for PZIII can be

determined by conducting some laboratory tests for other types of soil. The initial porosity, saturation of seabed soil used in the computation were 0.25, and 98 %, respectively. Correspondingly, the initial permeability of seabed soil was 1.0×10^{-5} m/s. The initial water depth of sea water over seabed floor was 10 m. In FEM discretization, a total of 4000 4-node elements, and 8282 solid and fluid nodes were used. The horizontal mesh size was 2 m, and the vertical meshsize was 0.5 m. The constant time step = 0.005 s was used. Totally, 60,000 time steps were implemented in the computations.

In offshore environments, the seabed soil generally has experienced a long-term consolidation process under hydrostatic pressure. There is no any excess pore pressure in seabed soil before a seismic wave arrives. This initial consolidation state of seabed soil is determined first (Ye 2012b). Then, this consolidation state is taken as the initial condition for the following seismic analysis.

Acceleration of the seabed

Due to the fact that the computational domain is symmetrical along $x = 100$ m, the results on $x = 100$ m monitored in the computation are taken as the representatives to illustrate the seismic dynamics and liquefaction mechanism in a loose seabed.

Figure 2 shows the time history curve of the response acceleration at the surface of the seabed ($x = 100$ m, $z = 20$ m). In Fig. 2, it can be seen that the PGA in the horizontal direction was only 0.07 g; while, it was 0.4 g in the vertical direction, which is much greater than that in the horizontal direction. It is indicated that the energy carried
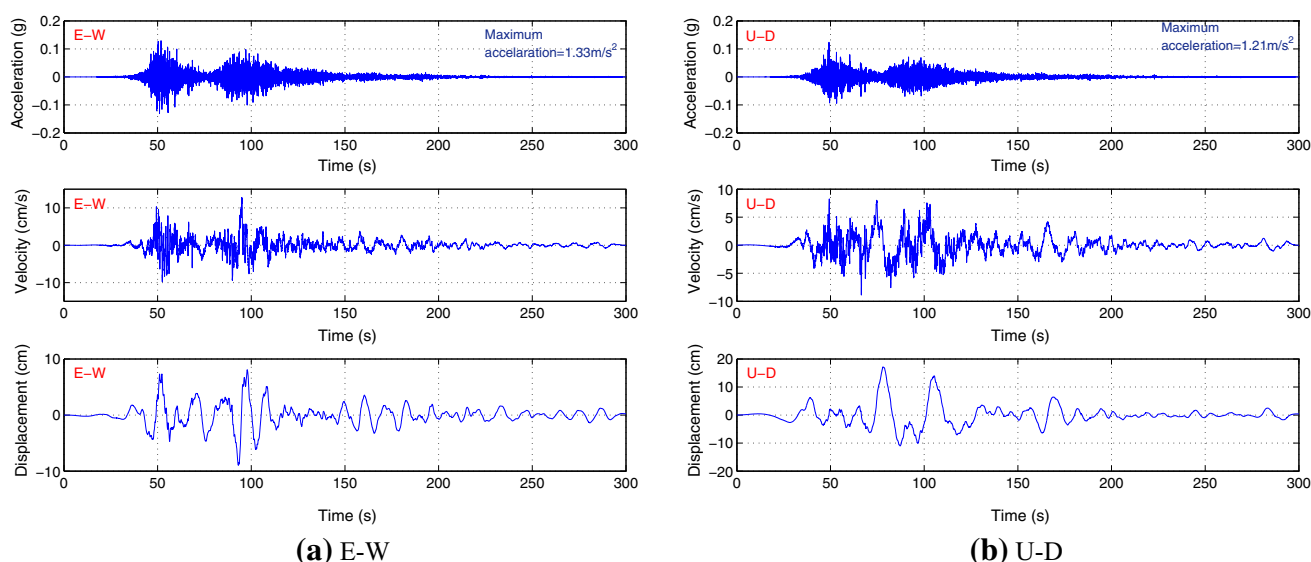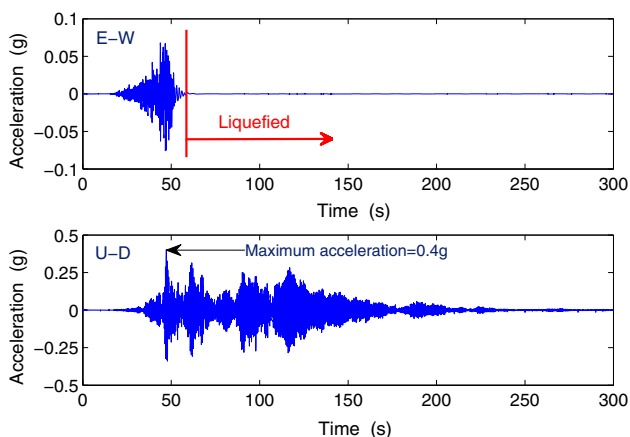

(a) E-W

(b) U-D

Fig. 1 Input seismic wave after wave filtering, adopting the recorded underground seismic wave at the station MYGH03 in Japan during the 311 off-Pacific earthquake event. *Note*: a noncausal Butterworth filter was used; filtering range: $f \leq 0.03$ Hz and $f \geq 30$ Hz

Table 1 Model parameters of a seabed foundation for PZIII in a seismic analysis

Item	Nevada dense sand	Unit
K_{evo}	2000	kPa
G_{eso}	2600	kPa
p'_0	4	kPa
M_g	1.32	–
M_f	1.3	–
α_f	0.45	–
α_g	0.45	–
β_0	4.2	–
β_1	0.2	–
H_0	750	–
H_{U0}	40,000	kPa
γ_u	2.0	–
γ_{DM}	4.0	–

by E–W seismic waves is significantly damped by the loose seabed soil. However, the vertical component of the input seismic wave is amplified in the loose seabed soil. This phenomenon can be clearly observed in Fig. 3, which demonstrates the vertical distribution of the PGA along the seabed depth. In Fig. 3, it is found that the PGA in the E–W direction, basically, is not amplified by the loose seabed; while, the PGA in U-D direction, basically, is linearly amplified by the loose seabed. On the surface of seabed soil, this amplification effect for the U–D component of the input seismic wave is most obvious. The PGA in the U–D direction at the surface of the seabed is 0.4 g, nearly four times the maximum input acceleration in the U–D direction.

It is interesting to observe another phenomenon in Fig. 2, that there is no horizontal response acceleration at ($x = 100$ m, $z = 20$ m) after $t = 60$ s. However, the vertical response acceleration at ($x = 100$ m, $z = 20$ m) after $t = 60$ s still exists. The subsequent analysis indicates that the reason for this phenomenon is the seismic wave-induced liquefaction occurring in the loose seabed. At time $t = 60$ s, part of the seabed layer has been completely liquefied. As we know, a liquefied seabed soil behaviors like a kind of heavy fluid, and completely loses its bearing capacity. Additionally, a shear wave can not be transmitted by liquefied soil. In this study, the input E–W component at the bottom of computational domain likes a shear wave. Once the loose seabed becomes liquefied, the E–W seismic wave will disappear in the seabed. Oppositely, the input U–D component behaves like a longitudinal wave (also referred to as a P wave), which can be transmitted in liquefied soil. That is the reason why the U–D component of response acceleration still exists after $t = 60$ s.

The acceleration response spectrum is an important basis for understanding the vibration characteristics of a loose seabed. The occurrence or not of resonance could be observed from an acceleration response spectrum. Figure 4 illustrates the acceleration response spectrum of the loose seabed at two typical positions ($x = 100$ m, $z = 20$ m) and ($x = 100$ m, $z = 10$ m). In Fig. 4, it is clearly seen that all frequency components of the horizontal input seismic wave, basically, were not amplified by the loose seabed; and the components with a frequency of 0.5–20 Hz in the vertical input seismic wave were significantly amplified by the loose seabed. The maximum response acceleration was 2.4 g and 1.6 g, both at a frequency of 1.7 Hz. Based on this, it is inferred that the natural frequency of the loose seabed could be 1.7 Hz.

Displacement of the seabed

Displacement is a direct indicator of the deformation of a seabed. The deformation characteristics of the Quaternary loose seabed under seismic wave loading is analyzed in this section. Figure 5 illustrates the time history curve of the seismic wave-induced displacement at the surface of the seabed. As illustrated in Fig. 5, there is only vertical subsidence before the time $t = 50$ s. After $t = 60$ s, the residual downward subsidence, basically, remained constant. There was only oscillatory vertical displacement. However, the seabed displaces to the right side after $t = 50$ s. The maximum horizontal displacement (24 cm) was reached at $t = 90$ s. The subsequent analysis on liquefaction indicates that this displacement mode of loose seabed is closely related to the seismic wave-induced liquefaction. The subsequent analysis shows that the upper seabed $z = 15$–20 m became liquefied at $t = 50$ s. Once

Fig. 2 Time history curve of the response acceleration at the surface of the seabed ($x = 100$ m, $z = 20$ m)

Fig. 3 Vertical distribution of PGA along seabed depth. It is shown that PGA in the horizontal direction, basically, is not amplified; while, PGA in vertical direction, basically, is linearly amplified by the loose seabed
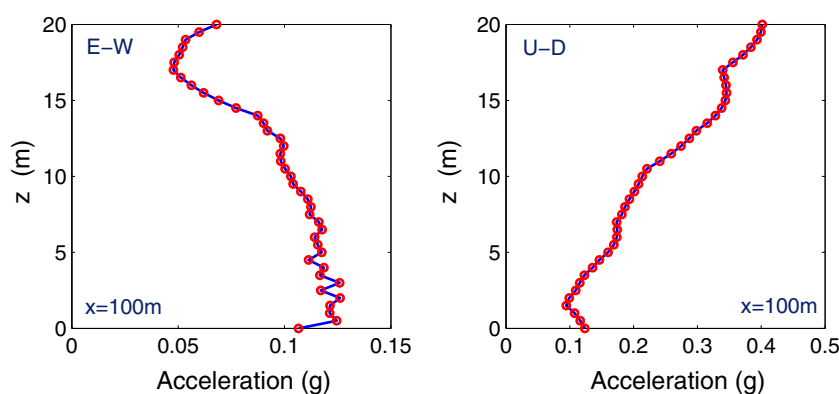
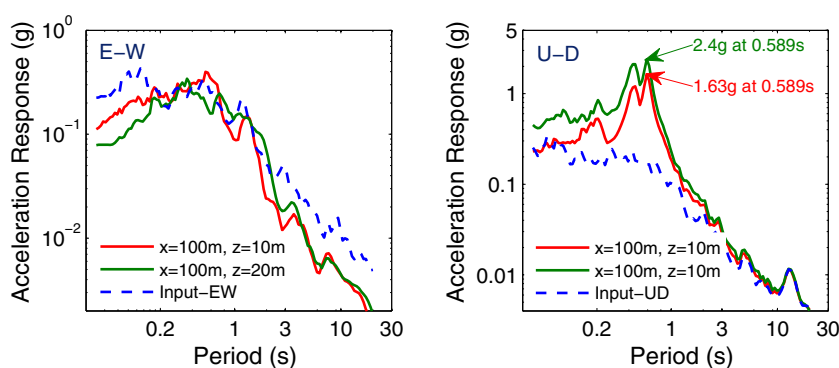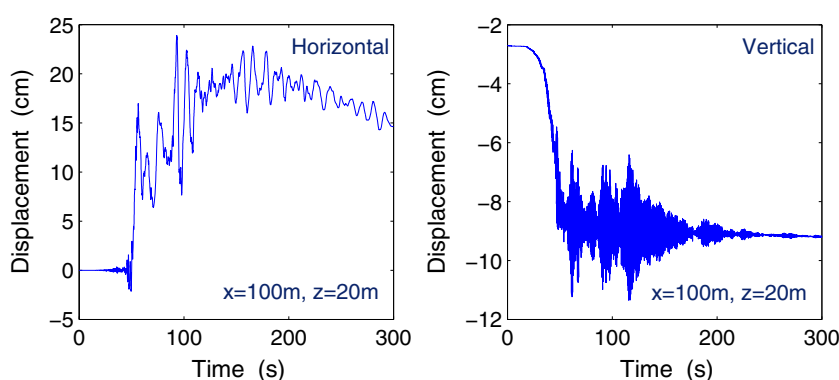Fig. 4 Acceleration response spectrum of a Quaternary seabed at typical positions

Fig. 5 Time history curve of seismic wave-induced displacement at ($x = 100$ m, $z = 20$ m)

part of the upper seabed liquefies, the seabed soil in the liquefied zone begins to flow to the right side. It is worth mentioning that seismic wave-induced horizontal displacement of a loose seabed is apparently small relative to the dimension of the computational domain. The subsequent analysis also shows that the whole loose seabed became liquefied after $t = 60$ s. Correspondingly, the downward residual subsidence in the seabed stops increasing in the liquefaction state. The reason for this phenomenon is the fact that the soil particles in liquefied soil are all suspended in pore water. There is, basically, no soil compaction inducing downward subsidence. Of course, this downward subsidence of seabed soil will gradually

increase again, accompanying the consolidation process after the seismic wave has left the chosen computational domain.

Figure 6 demonstrates vertical distribution of the seismic wave-induced displacement along seabed depth at the end of seismic wave loading. In Fig. 6, it is found that the vertical distribution of displacements along the seabed depth are both nonlinear; and the maximum horizontal and vertical displacements both occur at the surface of the seabed floor. The magnitude of displacements are oppositely related to the buried depth of seabed soil. Figure 7 shows the distribution of seismic wave-induced displacements in the whole seabed at time $t = 300$ s. Figure 7

indicates that the distribution of seismic wave-induced displacement is layered in the seabed. This is mainly attributed to the symmetry of the computational domain, as well as the periodical boundary on the lateral sides. It is indicated that the selection of results on $x = 100$ m as the representatives in the analysis is reasonable.

Pore pressure and effective stresses

The liquefaction in a loose seabed is closely related to the build-up of pore pressure and the reduction of effective stresses. Under seismic wave loading (a kind of cyclic loading), the soil particles in a loose seabed would rearrange their relative position to a more dense state, accompanying the drainage process. In this process, the pore pressure builds up quickly. It directly leads to the reduction of contractive effective stresses between soil particles. Once the excessive pore pressure overcomes the overburdening soil weight at a particular place, the soil becomes liquefied. Figures 8 and 9 illustrate the time history curve of pore pressure and the mean effective stresses at two typical positions on symmetrical axes $x = 100$ m.

In Figures 8 and 9, it can be observed that the pore pressure builds up quickly after the seismic wave arrives at the computational domain. Correspondingly, the effective stresses between soil particles reduce quickly. At an approximate time of $t = 60$ s, the residual pore pressure, basically, reaches its peak value. After $t = 60$ s, the residual pore pressure, basically, keeps a constant. There is only oscillative pore pressure. At the moment when the residual pore pressure reaches its peak value, the mean effective stress at the two typical positions decreases to zero. It means that the seabed soil becomes liquefied at this moment. After the initiation of liquefaction, the seabed soil always keeps this liquefaction state until the end of the seismic wave (the mean effective stress remains zero after $t = 60$ s). It is indicated that the pore pressure dissipation is apparently slow. Due to the fact that a liquefied soil

behaves like a heavy fluid; it can not transmit a shear wave. The shear stress between soil particles becomes zero once the seabed soil is liquefied. These two time history curves show that the constitutive soil model PZIII could describe the post-liquefaction behaviors of soil to some extent.

In offshore areas, the surface of the seabed is a natural draining boundary for pore water in loose seabed soil. After the input seismic wave arrives at the computational domain, the pore pressure in a loose seabed builds up quickly. It results in the formation of excessive pore pressure in the seabed. Accordingly, there is a pore pressure gradient between the surface of the seabed and places within the seabed. As a result, the pore water in loose seabed soil flows out through the surface of the seabed. After the seabed soil becomes liquefied, the pressure gradient, due to the seismic wave-induced residual pore pressure, reaches its maximum value. Accompanying the flowing out of pore water, the loose seabed soil compacts to a more dense state because of rearrangement of the soil particles. In this process, void ratio e of the soil decreases. It is noted that the reduction of void ratio e of soil is nonlinear. Figure 10 illustrates the time history curve of the seepage speed q of pore water through the seabed surface, and the accumulative discharge Q of pore water under the seismic wave loading. In Fig. 10, we can see that the seepage speed of pore water increases quickly from zero to its peak value in the process of pore pressure build up. After the seabed soil becomes liquefied, the seepage speed due to the residual pore pressure, basically, remains constant, about 1.2×10^{-5} m^3/s on one square meter area. The accumulative discharge Q of pore water from seabed to seawater increases linearly with time. Finally, about 3 L of pore water is discharged by the loose seabed on one square meter area.

Figure 11 demonstrates the distribution of pore pressure and the mean effective stress in the loose seabed at three typical times $t = 40$ s, $t = 60$ s and $t = 100$ s. An obvious characteristics of these distributions is that they are all layered. At $t = 40$ s, the mean effective stress in the seabed

Fig. 6 Vertical distribution of seismic wave-induced displacement along seabed depth at time $t = 300$ s
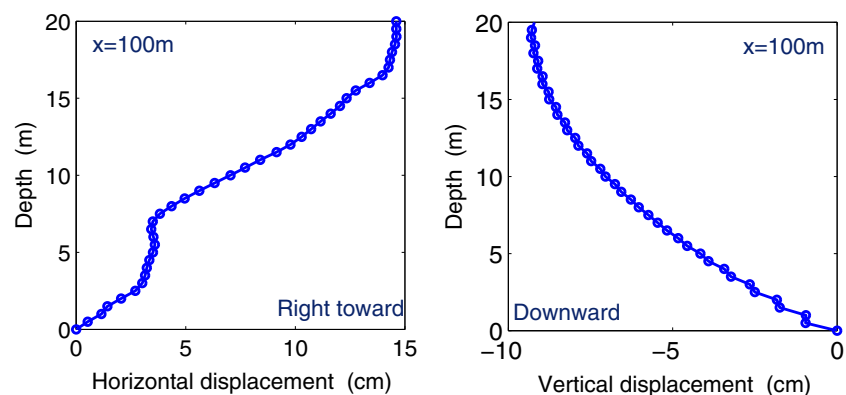
Fig. 7 Distribution of seismic wave-induced displacement in the seabed at time $t = 300$ s
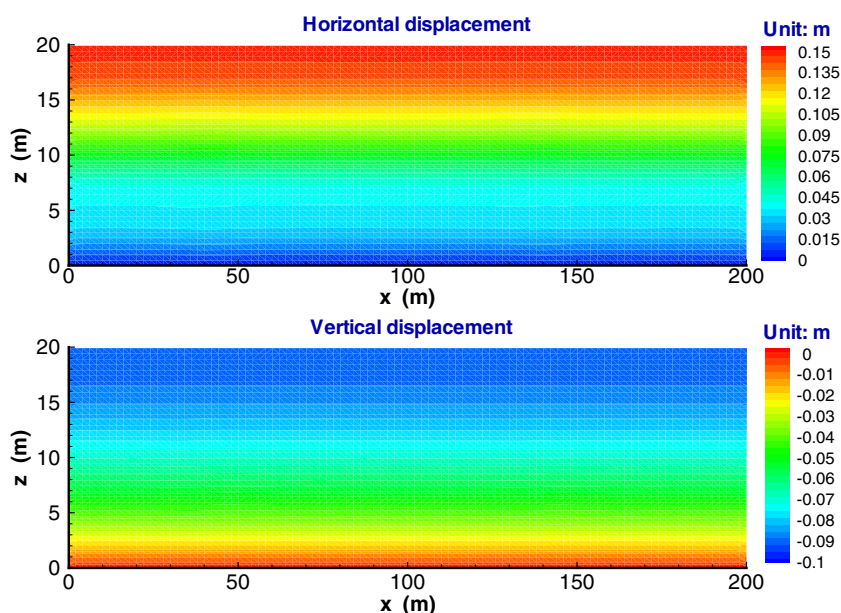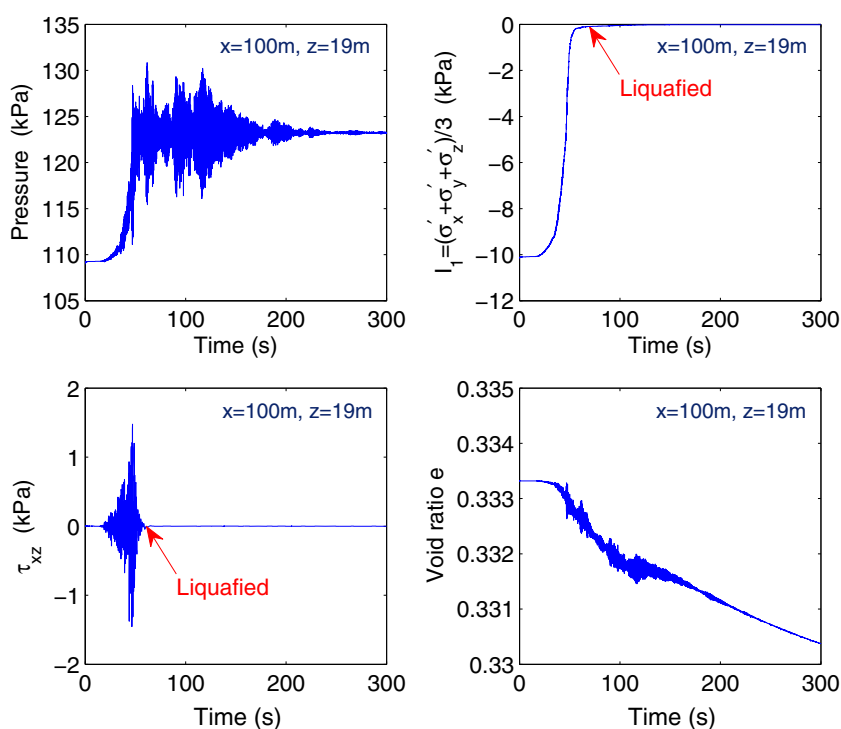

Fig. 8 Time history curve of pore pressure and effective stresses at a typical position ($x = 100$ m, $z = 19$ m)

is far from a zero-stress state. At $t = 60$ s, the pore pressure increases significantly, especially in the lower seabed. The mean effective stress in the seabed, generally, is <200 Pa, a value very close to a zero-stress state. It is indicated that the whole seabed, basically, is liquefied at $t = 60$ s. At $t = 100$ s, the pore pressure, basically, is the same with that at $t = 60$ s. However, the mean effective stress in the seabed is much more close to a zero-stress state. It is indicated that the liquefaction state of seabed soil is always

preserved after $t = 60$ s. It is interesting to observe that there is a thin layer at the seabed surface zone in which the mean effective stress is about 400–500 Pa when $t = 100$ s. This phenomenon is attributed to the fact that the pore pressure build up and dissipation exist simultaneously in a seabed under seismic wave loading. After $t = 60$ s, the pore pressure stops building up; meanwhile, the pore pressure dissipation in the seabed surface zone is significant. As a result, the effective stresses in the seabed surface

Fig. 9 Time history curve of pore pressure and effective stresses at a typical position ($x = 100$ m, $z = 10$ m)
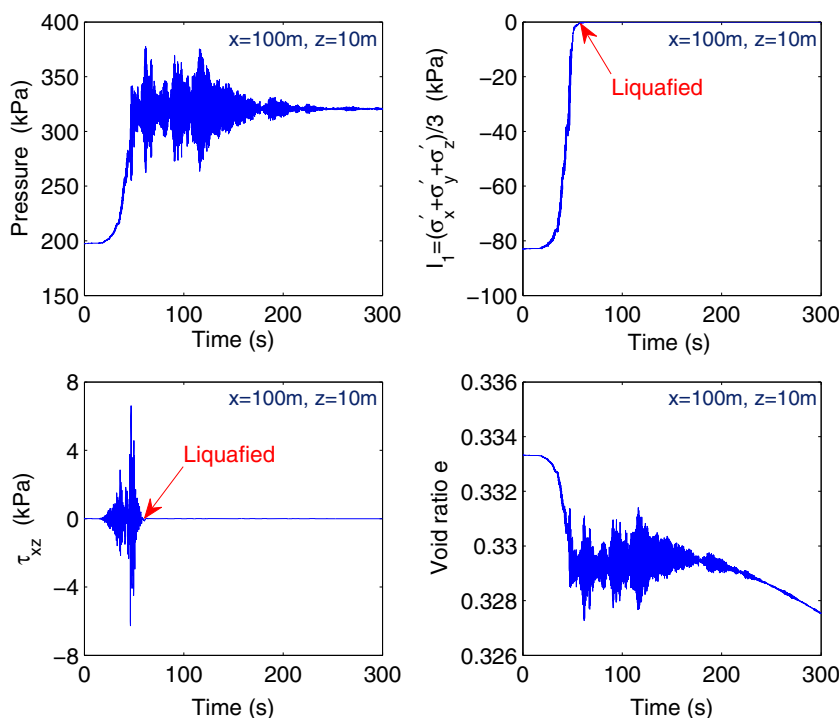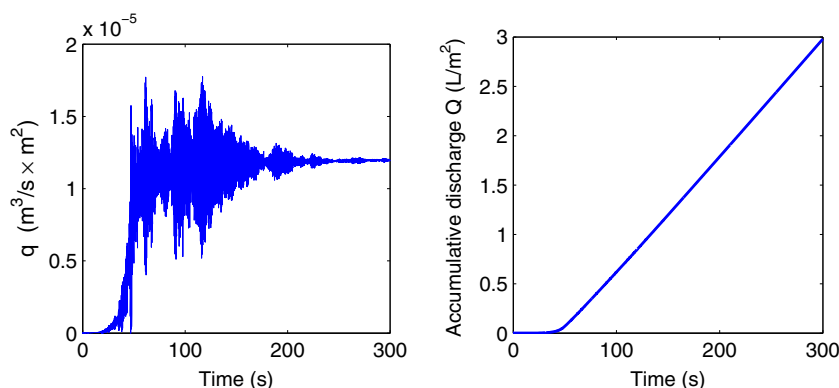

Fig. 10 Time history curves of seepage speed q and cumulative discharge Q

zone increase. This phenomenon provides us with a basis to infer the soil consolidation after liquefaction first occurs at the seabed surface zone, and propagates downward progressively.

Nonlinear stress–strain relation

Under the seismic wave loading, the loose seabed soil showed a nonlinear mechanical behavior. Figure 12 illustrates the nonlinear stress–strain relation at three representative positions on $x = 100$ m. They are ($x = 100$ m, $z = 19$ m) at the upper seabed, ($x = 100$ m, $z = 10$ m) at the middle seabed and ($x = 100$ m, $z = 5$ m) at the lower seabed. In Fig. 12, we can see that the stress–strain relation

was nearly linear at the beginning stage of seismic wave loading. After that, hysteresis loops appeared in the stress–strain curves due to the softening or liquefaction of the seabed soil. The shear modulus G of seabed soil gradually decreases in the process of liquefaction. Additionally, cyclic mobility occurs at the middle seabed. The peak shear strain at the middle seabed was about 2.2 %. At the lower seabed, the shear strain flows after the seabed soil becomes liquefied (shear stress $\tau_{xz} = 0$). The τ_{xz}-ϵ_v curves in Fig. 12 indicate that the loose seabed soil was contractive under seismic wave loading; and the magnitude of volumetric strain ϵ_v positively increases with buried depth. It was also observed that there is still variation of volumetric strain even after the seabed soil was liquefied.
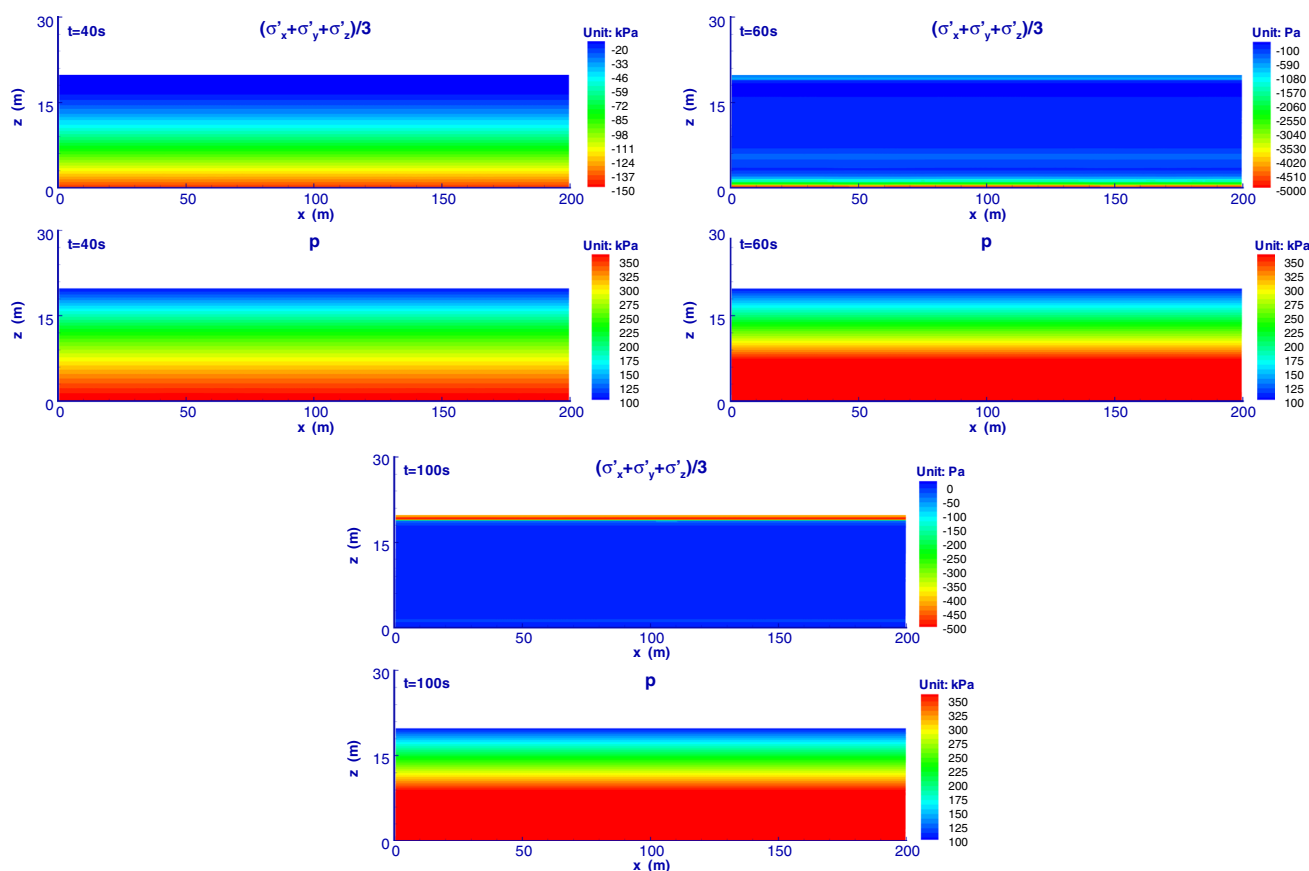
Fig. 11 Distribution of pore pressure and mean effective stress in a seabed at three typical times

Progressive liquefaction of seabed

It has been widely recognized that loose soil could liquefy under seismic wave loading. There are, generally, two types of liquefaction mechanisms for seabed soil. One is momentary liquefaction, only occurring in very dense sand. Another is residual liquefaction due to pore pressure build up in loose soil. The liquefaction occurring in Quaternary loose seabed soil in this study is exactly the residual liquefaction. Previous investigations by Sassa and Sekiguchi (1999) and Sassa and Sekiguchi (2001) showed that the ocean wave-induced liquefaction in loose seabed initiated at the surface of the seabed, and then progressively moved downward. However, for the seismic wave-induced liquefaction in a loose seabed, the understanding on where it initiates, and whether it is also progressive or not, is limited. In this section, the seismic wave-induced residual liquefaction in the Quaternary loose seabed soil is intensively investigated. The above-mentioned two questions: where it initiates, and whether it is progressive, will be quantitatively asked.

Figure 13 shows the vertical distribution of the seismic wave-induced residual pore pressure along the seabed depth at different times. It is shown that there was no

excessive pore pressure at $t = 0$ s. After the seismic wave arrived at the computational domain, the residual pore pressure increased significantly with time. However, there was no residual pore pressure at the surface of the seabed ($z = 20$ m) at anytime. The magnitude of residual pore pressure at one time, basically, is positively related to the buried depth.

It is interesting to find that the residual pore pressure after $t = 60$ s can not build up continuously. There is a limit line to constrain the build up of residual pore pressure after $t = 60$ s. More detailed observation finds that this limit line is the gravity-induced stress line $\sigma'_z = \gamma_s \times z$ of the seabed soil. The unit weight of seabed soil γ_s is about 12 kN/m³. According to the definition of liquefaction of soil, the seabed soil becomes liquefied if the residual pore pressure reaches the gravity stress line. After seabed soil liquefies, the residual pore pressure in it can not continue to increase. Therefore, the residual pore pressure can not increase infinitely in seabed soil. At about $t = 60$ s, the seabed soil basically liquefies completely.

More detail information about the build up of residual pore pressure in the period $t = 50$–60 s is also demonstrated in Fig. 13. It can be clearly seen that the residual

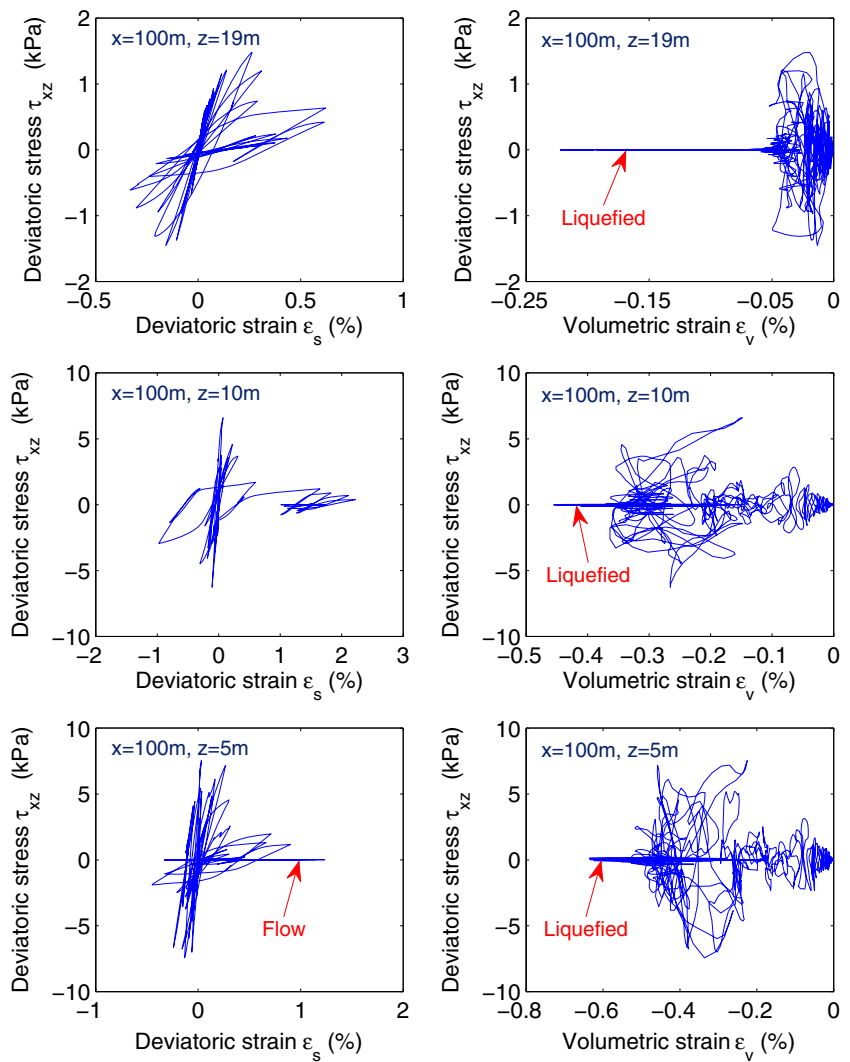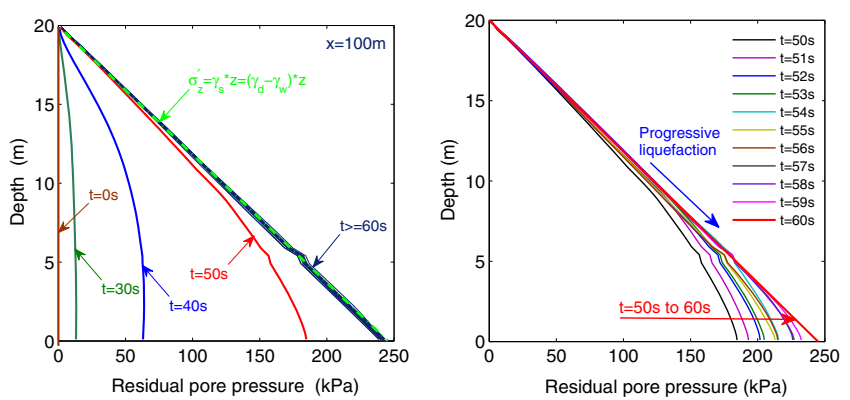**Fig. 12** Nonlinear stress–strain relation at three typical positions on a symmetrical axis $x = 100$ m

Fig. 13 Vertical distribution of residual pore pressure along seabed depth at different times. $\gamma_s^* = 12$ kN/m³

pore pressure didnot reach the gravity stress line at one time, but gradually with time. The residual pore pressure reached the gravity stress line firstly in the upper seabed, then in the lower seabed. From this phenomenon, it is inferred that the seismic wave-induced liquefaction in

loose seabed is also progressive downward, as that induced by ocean waves.

Apart from residual pore pressure, the effective stress path also can be used to describe the liquefaction process of soil. Figure 14 illustrates the stress path at several typical

positions on $x = 100$ m. In Fig. 14, it is shown that the initial stress states are all on the k_0 line ($k_0 = 0.5$). Under the seismic wave loading, the stress paths all nonlinearly moved toward the zero stress point, which is the symbol of soil liquefaction. Figure 14 shows that all stress paths on these typical positions finally reached the zero stress point. It is indicated that the soil at these positions finally became liquefied under seismic wave loading. Figure 14 indicates that the liquefaction of soil is also a complex process.

Herein, the progressive process of seismic wave-induced soil liquefaction was quantitatively investigated. Generally, there are three types of liquefaction criteria for judging the occurrence of liquefaction. They are based on residual pore pressure, effective stress (Ye et al. 2013) and accumulative shear strain (Wu et al. 2004). The criteria based on accumulative shear strain is highly dependent on soil types and loading characteristics. Here, only the criteria based on residual pore pressure and effective stress were used.

Figure 15a shows the predicted liquefaction process adopting the residual pore pressure-based liquefaction criteria. It is clearly observed that the soil liquefaction initiated at the surface of the seabed, and then progressively moved downward. At about $t = 62$ s, the loose seabed becomes completely liquefied.

The effective stress-based liquefaction criteria deems the seabed soil is liquefied when the contact effective stress between soil particles reaches zero. However, the reality is that it is impossible for the effective stress between soil particles in numerical modelling to become zero, but they can reach a very small value, such as 1.0×10^{-15} Pa. Additionally, the seabed soil begins to flow like a kind of heavy fluid before the effective stress approaches zero. In some engineering practices, soil is deemed to be liquefied when the effective stress decreases to 10–15 % of the initial effective stress. Therefore, the strict definition of liquefaction ($\sigma'_z = 0$), basically, is not applicable. Here, several critical values were chosen to illustrate the

progressive liquefaction process based on effective stress. Figure 15b illustrates the predicted liquefaction process adopting the effective stress-based liquefaction criteria, in which five different critical values were used. It is also shown that the seismic wave-induced liquefaction also initiates at the surface of the seabed, and then progressively moves downward. The biggest difference between the five predicted liquefaction process curves is the time for initiation, and the time in which the seabed liquefies completely is different. Regardless which critical value is chosen, the seabed becomes completely liquefied not later than $t = 70$ s. Another regulation is that the greater the critical value for effective stress, the earlier the initiation of the soil liquefaction at the surface of the seabed.

Effect of lateral boundary condition

In this study, the laminar lateral boundary condition is applied on the two lateral boundaries of the computational domain. The laminar boundary condition makes the seabed soil deform freely on the lateral sides of the computational domain (actually, it is a periodical boundary). Equivalently, the seabed is infinite in the horizontal direction. There is no wave reflection on the lateral sides of the computational domain. Clearly, a laminar boundary is more close to the real situation in offshore environments. Generally, there is another lateral boundary–fixed lateral boundary frequently used in computations. A fixed lateral boundary condition is similar to the boundary condition involved in shaking table tests. There is wave reflection on the fixed lateral boundary. Here, the effect of the two types of boundary conditions on the seismic dynamics of a loose seabed is discussed.

Figure 16 illustrates the comparison of seismic dynamics of a seabed, adopting the laminar boundary and fixed boundary. In Fig. 16, it is found that the horizontal displacement ($t = 300$ s) on $x = 100$ m is significantly different when the two types lateral boundary conditions are respectively used in computation. However, the vertical displacement ($t = 300$ s), basically, is the same. As analyzed in the above section, the seabed soil significantly displaces to the right side after the seabed soil is completely liquefied when a laminar boundary condition is applied. However, the lateral displacement is constrained by the fixed lateral sides when a fixed boundary condition is applied. This difference in horizontal displacement is reasonable and explainable. The magnitude of difference is within 20 cm, which is apparently small relative to the horizontal dimension of the computational domain.

The comparison on peak acceleration in Fig. 16 shows that there is only a minor difference in horizontal peak acceleration. The vertical peak acceleration is exactly the
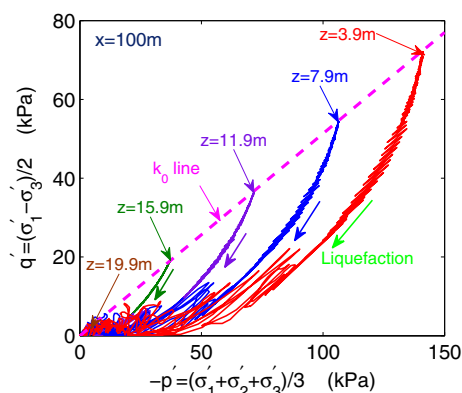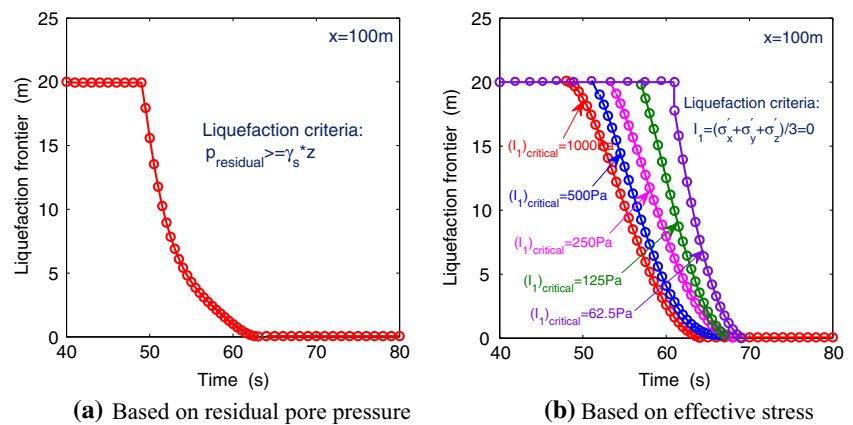

Fig. 14 Stress paths at several typical positions on a symmetrical line $x = 100$ m ($k_0 = 0.5$)

Fig. 15 Predicted progressive liquefaction process of a seabed under seismic wave loading ($\gamma_s = 12$ kN/m^3)

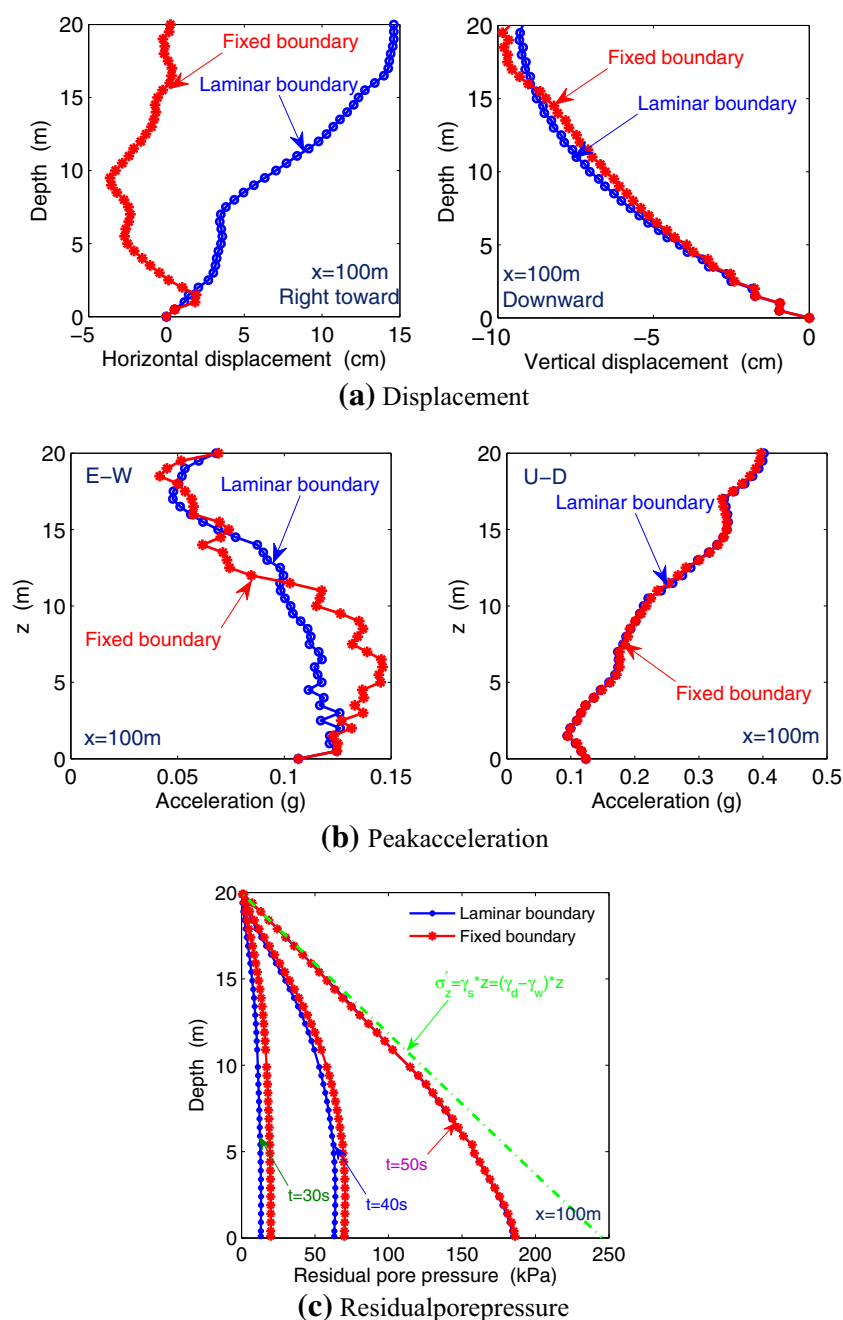**(a)** Based on residual pore pressure

(b) Based on effective stress

same when the two types of lateral boundaries are respectively applied. The comparison of residual pore pressure, which is the key factor resulting in seabed soil liquefaction, shows that the difference is visible before $t = 50$ s. At $t = 50$ s, the difference on residual pore pressure disappears. Overall, a fixed lateral boundary has some slight effect on the horizontal seismic dynamics of seabed, and on the residual pore pressure before $t = 50$ s. Finally, it is concluded that a fixed lateral boundary condition could be applicable in numerical modelling of seismic dynamics of a seabed; however, it is suggested that the horizontal dimension of the computational domain could be lengthened moderately, to eliminate the effect of the lateral boundary condition on numerical results as best as possible.

Conclusion

In this study, the seismic dynamics of a loose Quaternary seabed in an offshore environment and the seismic wave-induced liquefaction mechanism were investigated, adopting the coupled FEM numerical model FSSI-CAS 2D. The dynamic behaviour of the loose Quaternary seabed soil was modelled by a widely validated soil constitutive model—the Pastor–Zienkiewicz Mark III (PZIII) model proposed by Pastor et al. (1990), which is one of the heritages of Zienkiewicz (Pastor et al. 2011). In this numerical investigation, the variation of the void ratio, the corresponding permeability of the seabed soil, and the hydrostatic pressure on the seabed floor was updated according to the deformation of the seabed soil. Numerical results indicate that the developed numerical model FSSI-CAS 2D is capable of capturing a variety of nonlinear physical mechanisms of seismic dynamics of a seabed in offshore environments. After careful consideration, the following conclusions are made:

1. Under strong seismic wave loading, a loose seabed could be liquefied quickly, accompanying the pore pressure build up. Computational results show that liquefied seabed soil behaves like a heavy fluid. Shear waves can not be transmitted in liquefied seabed soil. This phenomenon proves, to some extent, that the soil constitutive model PZIII is capable of describing the post-liquefaction behaviour of soil for some cases.

2. It is found that the PGA in the E–W direction, basically, is not amplified by the loose seabed; while, the PGA in the U–D direction, basically, is linearly amplified by the loose seabed. This is significantly different with that of a very dense seabed, in which the E–W input seismic wave is also significantly amplified.

3. In the process of soil liquefaction induced by seismic waves, the loose seabed become more and more dense, accompanying the drainage and subsidence of the seabed.

4. Seismic wave-induced liquefaction in a loose seabed is also progressive as that induced by ocean waves. It initially occurs at the surface of the seabed, and then the frontier of the liquefaction zone progressively moves downward. Essentially, there is no special difference in the liquefaction mechanism in loose seabed soil triggered by seismic waves or water waves. Regardless of being triggered by seismic waves or water waves, the occurrence of liquefaction in loose seabed soil is due to pore pressure build up, resulting from the cyclic shearing on granular materials. However, due to the fact that the disturbance energy carried by seismic waves, generally, is much greater than that applied by water waves, the seismic wave-induced liquefaction in loose seabed is much faster than that induced by water waves; and the liquefaction depth could easily reach 20 m. As a comparison, Ye et al. (2015) showed that the standing water wave-induced

Fig. 16 Effect of the lateral boundary condition on the seismic dynamics of a seabed ($t = 300$ s)

(a) Displacement

(b) Peakacceleration

(c) Residualporepressure

liquefaction depth in the same seabed soil is only about 8 m after $t = 45\,T$ loading (wave height $H = 6.0$ m, water depth $d = 15$ m, wave period $T = 8.0$ s).

5. A laminar lateral boundary condition is more representative of a real seabed in an offshore environment. However, a fixed lateral boundary condition also could be applicable in numerical modelling of the seismic dynamics of a seabed, when the horizontal dimension of the computational domain is lengthened moderately.

References

Bao X, Ye G, Ye B, Sago Y, Zhang F (2014) Seismic performance of SSPQ retaining wall‖centrifuge model tests and numerical evaluation. Soil Dyn Earthq Eng 61–62:63–82

Chan AHC (1988a) A unified finite element solution to static and dynamic problems of geomechanics. In: PhD thesis, University of Wales, Swansea Wales

Chan AHC (1988b) A unified finite element solution to static and dynamic problems of geomechanics. In: PhD thesis, University of Wales, Swansea Wales

Groot D, Bolton MB, Foray MD, Meijers P, Palmer AC, Sandven R, Sawicki A, Teh TC (2006) Physics of liquefaction phenomena around marine structures. J Waterw Port Coast Ocean Eng 132:227–243

Heider Y, Avci O, Markert B, Ehlers W (2014) The dynamic response of fluid-saturated porous materials with application to seismically induced soil liquefaction. Soil Dyn Earthq Eng 63:120–137

Hsu TJ, Sakakiyama T, Liu PLF (2002) A numerical model for wave motions and turbulence flows in front of a composite breakwater. Coast Eng 46:25–C50

Huang Y, Mao WW, Zheng H, Li GH (2012) Computational fluid dynamics modeling of post-liquefaction soil flow using the volume of fluid method. Bull Eng Geol Environ 71(2):359–366

Huang Y, Yashima A, Sawada K, Zhang F (2008) Numerical assessment of the seismic response of an earth embankment on liquefiable soils. Bull Eng Geol Environ 67(1):31–39

Huang Y, Yu M (2013) Review of soil liquefaction characteristics during major earthquake of the 21st century. Nat Hazards 65(3):2375–2384

Jafarian Y, Alielahi H, Abdollahi AS, Vakili B (2010) Seismic numerical simulation of breakwater on a liquefiable layer: IRAN LNG port. Electron J Geotech Eng 15D:1–11

Miyamoto J, Sassa S, Sekiguchi H (2004) Progressive solidification of a liquefied sand layer during continued wave loading. Géotechnique 54(10):617–629

Pastor M, Chan AHC, Mira P, Manzanal D, Fernndez MJA, Blanc T (2011) Computational geomechanics: the heritage of Olek Zienkiewicz. Int J Numer Meth Eng 87(1–5):457–489

Pastor M, Zienkiewicz OC, Chan AHC (1990) Generalized plasticity and the modelling of soil behaviour. Int J Numer Anal Methods Geomech 14:151–190

Sassa S, Sekiguchi H (1999) Wave-induced liquefaction of beds of sand in a centrifuge. Géotechnique 49(5):621–638

Sassa S, Sekiguchi H (2001) Analysis of wave-induced liquefaction of sand beds. Géotechnique 51(2):115–126

Sumer BM, Ansal A, Cetin KO, Damgaard J, Gunbak AR, Hansen NEO, Sawicki A, Synolakis CE, Yalciner AC, Yuksel Y, Zen K (2007) Earthquake-induced liquefaction around marine structures. J Waterw Port Coast Ocean Eng 133(1):55–82

Wang G, Sitar N (2011) Static and dynamic axial response of drilled piers. II: Numerical simulation. J Eng Mech ASCE 137(12):1143–1153

Wu J, Kammaerer AM, Riemer MF, Seed RB, Pestana JM (2004) Laboratory study of liquefaction triggering criteria. In: Proceedings of 13th world conference on earthquake engineering, Vancouver, British Columbia, Canada. Paper No. 2580

Xia ZF, Ye GL, HWang J, Ye B, Zhang F (2010) Fully coupled numerical analysis of repeated shake-consolidation process of earth embankment on liquefiable foundation. Soil Dyn Earthq Eng 30(11):1309–1318

Ye B, Ye GL, Zhang F, Yashima A (2007) Experimental and numerical simulation of repeated liquefaction-consolidation of sand. Soils Found 3(47):547–558

Ye JH (2012a) Numerical analysis of wave-seabed-breakwater interactions. In: PhD thesis, Universtity of Dundee, Dundee, UK

Ye JH (2012b) Numerical modelling of consolidation of 2-D porous unsaturated seabed under a composite breakwater. Mechanika 18(4):373–379

Ye JH (2012c) Seismic response of poro-elastic seabed and compositebreakwater under strong earthquake loading. Bull Earthq Eng 10(4):1609–1633

Ye JH, Jeng D-S (2013) Three-dimensional dynamic transient response of a poro-elastic unsaturated seabed and arubble mound breakwater due to seismic loading. Soil Dyn Earthq Eng 44:14–26

Ye JH, Jeng D-S, Wang R, Zhu C (2013) Validation of a 2-D semi-coupled numerical model for fluid–structure–seabed interaction. J Fluids Struct 42:333–357

Ye JH, Jeng D-S, Wang R, Zhu CQ (2015) Numerical simulation of wave-induced dynamic response of poro-elasto -plastic seabed foundation and composite breakwater. Appl Math Model 39(1):322–347

Ye JH, Wang G (2015) Seismic dynamics of offshore breakwater on liquefiable seabed foundation. Soil Dyn Earthq Eng 76:86–99

Zienkiewicz OC, Chan AHC, Pastor M, Schrefler BA, Shiomi T (1999) Computational geomechanics with special reference to earthquake engineering. Wiley, New York

Zienkiewicz OC, Chang CT, Bettess P (1980) Drained, undrained, consolidating and dynamic behaviour assumptions in soils. Geotechnique 30(4):385–395